3D CFD MODEL FOR THE ANALYSIS OF THE FLOW FIELD THROUGH A HORIZONTAL AXIS WIND TURBINE (HAWT)

NOUREDDUBE MENASRI*, SAID ZERGANE, NOUREDDINE AIMEUR, AISSA AMOUR

University of Mohamed Boudiaf M'sila, Faculty of Mechanical Technology, Laboratory of Materials and Mechanical Structures, B.P 166 Ichbilia, M'sila, 28000, Algeria

* corresponding author: `noureddine.menasri@univ-msila.dz`

ABSTRACT. With the world's growing demand for energy, renewable energy production has become important in providing alternative sources of energy and in reducing the greenhouse effect. This study investigates the aerodynamics and performance of the WG/EV100 micro–Horizontal Axis Wind Turbine (HAWT) using Computational Fluid Dynamics (CFD). The complexity of VAWT aerodynamics, which is inherently unsteady and three-dimensional, makes high-fidelity flow models extremely demanding in terms of computational cost, limiting the analysis to mainly 2D Computational Fluid-Dynamics (CFD) approaches. This article explains how to perform a full 3D unsteady CFD simulation of HAWT. All main parts of the WG/EV100 HAWT were designed in SOLIDWORKS. Only the blade design was reverse engineered due to the unavailability of the CAD model and the complexity of its geometric characteristics. The impeller blade is scanned using a Coordi-nate Measuring Machine (CMM), and the obtained 3D scan data are exported from the PC-DMIS software to GEOMAGIC design X to obtain a CAD model of the blade.

KEYWORDS: Computational Fluid Dynamics, Horizontal Axis Wind Turbine (HAWT), aerodynamics, reverse engineering, Coordinate Measuring Machine (CMM).

1. INTRODUCTION

Wind energy is a renewable energy source that promotes diversification and energy independence in the electricity generation industry [1–5]. It is clean energy that does not produce greenhouse gases. It uses machines with a life cycle that respects the environment. It is decentralised energy and the energy-producing machines can be closer to consumers. There is an immense potential and an inexhaustible source of renewable energy in the world allowing for a diversification of energy sources. This is the reason why this type of energy has now become a recommendation from the public authorities, an essential source for the very near future, and an alternative strategy for fossil fuels.

Wind turbines can be divided into two main categories, Horizontal Axis Wind Turbines (HAWT) and Vertical Axis Wind Turbines (VAWT). HAWT have the axis of rotation of their blades horizontal to the ground and almost parallel to the wind stream, while VAWT have the axis of rotation and blades oriented vertically [6–8].

A typical HAWT consists of major components including blades, rotor, nacelle unit, tower, and gearbox. The blades, as one of the key components of wind turbines, cost about 20 % of the machine. Their proper design, reliable quality, and superior performance are critical factors in improving the utilisation rate of wind energy and ensuring a stable operation of wind turbines.

Among the methods for designing the blade profile, we can mention the method of direct design of the aero-dynamic profiles of wind turbines based on mathematical optimisation [9–11] and the XFOIL software from RISO [12], the PARSEC (Pseudo potential Algorithm for Real-Space Electronic Calculations) method for designing airfoils by controlling the airfoil geometry parameters [13], and the blade element moment method where the blade is modelled as a ruled 3D surface [14]. When the CAD model of the blade was not available, we used the reverse engineering method [15–19].

Much effort has been devoted to the research and development of large wind turbines to minimise specific costs (EUR kW^{-1}). Improved aerodynamic design and increased tower height and turbine size have allowed for a significant reduction in unit power generation costs [20].

The general equations of an engineering problem form a set of coupled and nonlinear partial differential equations. Solving such equations analytically is usually difficult or even impossible for most engineering problems, hence the need for a CFD application [21–24], which is a branch of fluid mechanics that uses numerical methods and algorithms to analyse and solve fluid flow problems [25].

A 2D CFD simulation is simpler compared to the 3D CFD simulation, but at the same time, it is less accurate for complex flow cases and is limited to a single plane case. A 3D CFD simulation provides an accurate prediction of the flow field, but requires a

long computation time and large data storage [26].

Meanwhile, the Blade Element Momentum (BEM) method can be used for the blade structure analysis. The BEM method consists of dividing the flow into annular control volumes and applying momentum balance and energy conservation in each control volume. These models can implement different analysis algorithms: the single-stream tube model, which considers one stream tube for the entire rotor, the multiple-stream tube model, which considers an arbitrary number of adjacent and aerodynamically independent stream tubes, and the double-multiple-stream tube model, where the rotor is represented by a pair of actuator discs in tandem on each stream tube [27].

Several studies have been developed to design and evaluate the performance of HAWTs. Ngala, G.M et al. [6–8], Younes El khchine, and Mohammed Sriti [28] have investigated the performance of a micro-HAWT blade using a combination of Computational Fluid Dynamics (CFD) and Blade Element Momentum Method (BEM) methods to simulate the flow field around a wind turbine rotor with horizontal axis in 2D. The result shows that the power output increases consistently with increasing wind speed.

Hasan et al. [29] and Khaled et al. [30] have conducted a comparative study between BEM and CFD analysis of small-scale horizontal axis wind turbine blades. Both studies showed good a performance prediction which was a positive step to accelerate the continuous development in the wind energy sector. Chandrala et al. [31] conducted a study on the aerodynamic efficiency of wind turbine blades in a wind tunnel. A CFD analysis of the HAWT blade at different blade angles was carried out using ANSYS CFX. They found that the HAWT efficiency is highly dependent on the blade profile and its orientation. Khlaifat et al. [32] have shown that the performance of a wind turbine is affected by the wind conditions and the blade shape.

Rossetti and Pavesi [33] compared the BEM approach with two-dimensional and three-dimensional CFD simulations. The curves of tip–speed ratio versus power coefficient and the evolution of the trust forces over one blade revolution highlighted the limitations and strengths of each approach.

Zhang et al. [34] investigated the effect of yaw speed and delay time on the power generation and stress of a wind turbine. The results show that the step control of the yaw speed can avoid power loss and improve the reliability of the wind turbine during operation.

Our research focuses mainly on investigating the aerodynamic performance of the WG/EV100 micro-HAWT using Computational Fluid Dynamics (CFD). All main parts of the WG/EV100 HAWT were designed in SOLIDWORKS. Only the blade design was reverse engineered due to the unavailability of the CAD model and the complexity of its geometric characteristics. The impeller blade is scanned using a Coordinate Measuring Machine (CMM), and the ob-
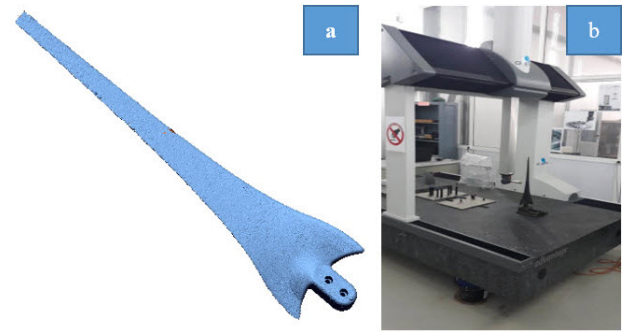

FIGURE 1. a) Cloud data from CMM. b) Impeller Blade.

tained 3D scan data are exported from the PC-DMIS software to GEOMAGIC design X to obtain a CAD model of the blade.

2. METHODOLOGY

2.1. 3D SCANNING OF A WIND TURBINE BLADE

In order to simulate the performance of the wind turbine under consideration, a numerical study of the three-dimensional flow is carried out by means of CFD using the commercial CFD code ANSYS Fluent. Due to the sensitivity of the flow field in the blade passage to the geometric properties of the blade, the CAD model of the blade was created using reverse engineering because of the lack of a 3D model of the wind turbine blade.

The reverse engineering technique was required to extract the geometric features from the physical model at different angles using a 3D scanner.

For reverse engineering purposes, the wind turbine blade was 3D scanned using a coordinate measuring machine (CMM) to create highly accurate 3D models. This process is critical for manufacturing replacement parts, improving the design of existing components, or repairing damaged components. The CMM used in this study has three axes and is highly capable of measuring large and complex geometries with a high level of precision ($1\,\mu$m) [35]. The scanning process involved a mechanical method using a tactile trigger probe to collect data by physically touching the blade surface in a predetermined pattern and generating a continuous stream of point cloud data. This ensured that the entire surface of the blade was scanned and any defects or variations in the shape of the blade were accurately captured. Once the scanning process was completed, the collected data were converted into a digital format using PC-DMIS software. This software allowed the collected data to be processed and analysed, ensuring that any imperfections or inaccuracies were corrected. The digitised data were then exported to Geomagic Design X software, which was used to generate the final CAD model.

As can be seen in Figure 1, the point cloud data of the wind turbine blade were extracted.
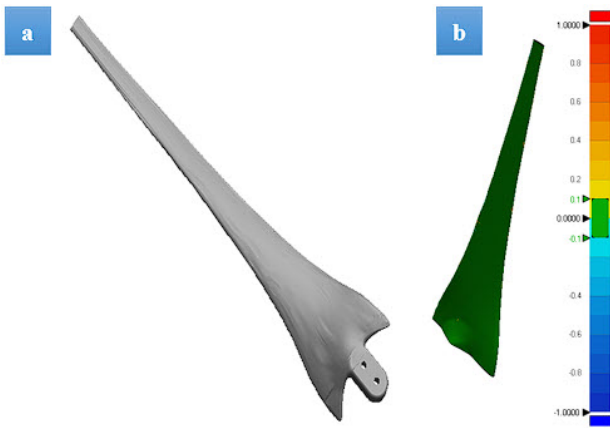
Figure 2. a) CAD model of the wind turbine blade. b) Deviation of the CAD model of the blade from the measured point cloud data.
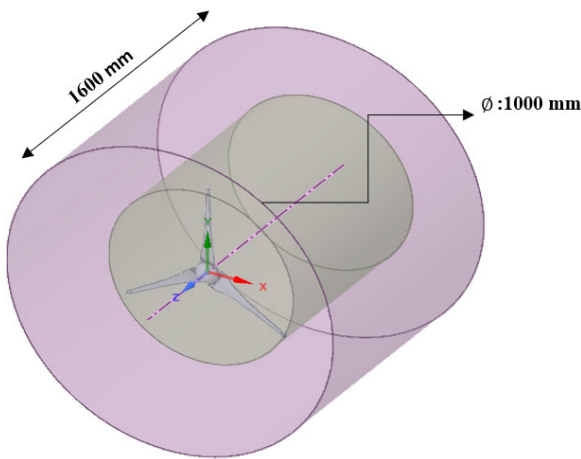

Figure 3. Wind turbine model.

By analysing the survey data, a robust design of a wind turbine was created that ensures its deflection on the cloud remains within ±0.1 mm. The CAD design is shown in Figure 2.

2.2. Geometric model

After reverse engineering the 3D model of the wind turbine blade, the CAD model can be processed by various CAD programs. For our specific study, we used SOLIDWORKS to create the CAD model. The ANSYS Space Claim program was used to generate the fluid domain that consists of cylindrical geometry with specific dimensions. Due to the complexity of the meshing, an inner cylinder was created as shown in Figure 3. In order to match the geometry input required for the CFD analysis by FLUENT software, the solid structures must be subtracted from the field using Boolean operations. Once the geometry is complete, it is imported into the AN-SYS FLUENT MESHING program to generate the mesh.

Because of the symmetric nature of the fluid domain, only one third of the entire cylinder was included in the simulation, as shown in Figure 4. This significantly
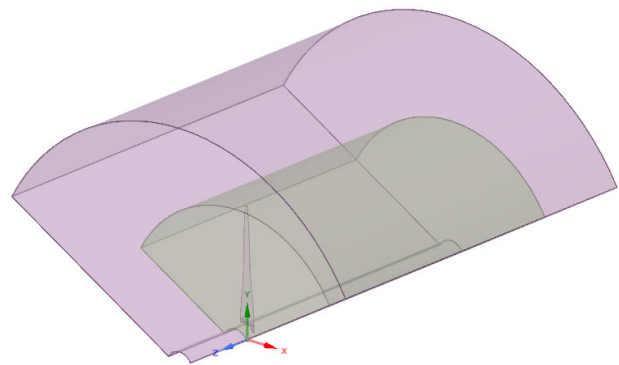
Figure 4. Arithmetic range of a wind turbine blade.

reduced the computational time and the calculating resources required for the simulation.

2.3. Meshing

Because ANSYS fluent supports a wide range of mesh types, a wide variety of tools, such as ANSYS Meshing, ICEM CFD, and CFX, it can be used to generate the mesh required for a fluid dynamics analysis. The mesh resolution was performed using the ANSYS fluent meshing program after the geometry was completed and imported into the fluent meshing program to create the mesh. The mesh is structured and consists of cells and nodes which can be of any shape and size.

It is assumed, based on a fundamental understanding of fluid mechanics, that the flow behind the blades of wind turbines is the most turbulent and that this is the location where a fine mesh is required to capture all the physical effects of the flow. The outflow is where the coarsest mesh is used because it is least affected by the wind turbine blades. This mesh resolution reduces the computational time without compromising the accuracy of the numerical results.

A cylindrical computational domain was performed without a large and unnecessary re-meshing process, since the flow was symmetric and the rotating blades were determined periodically, only one blade was connected using the 120° periodic feature of the third model to reduce the computational cost, and thus the computational domain consists of one blade. In the third axis, we used two types of fields, the inner field containing the wind turbine blade with a fine mesh and the outer field surrounding it with a coarse mesh. To ensure mesh independence, we performed successive mesh refinements and simulations. During steady state simulations, we monitored the moment around the Z-axis to perform a mesh sensitivity analysis. The mesh refinement was focused on the blade and followed a smooth transition from low to high mesh density. We determined that fur-ther refinement was unnecessary once the grid surpassed 6 494 745 nodes, as it would be computationally inefficient. Ultimately, we used 5 574 675 poly-hex core cells to achieve a mesh-independent solution. A computational mesh and the inflation layers on the blade surface are shown in Figure 5.
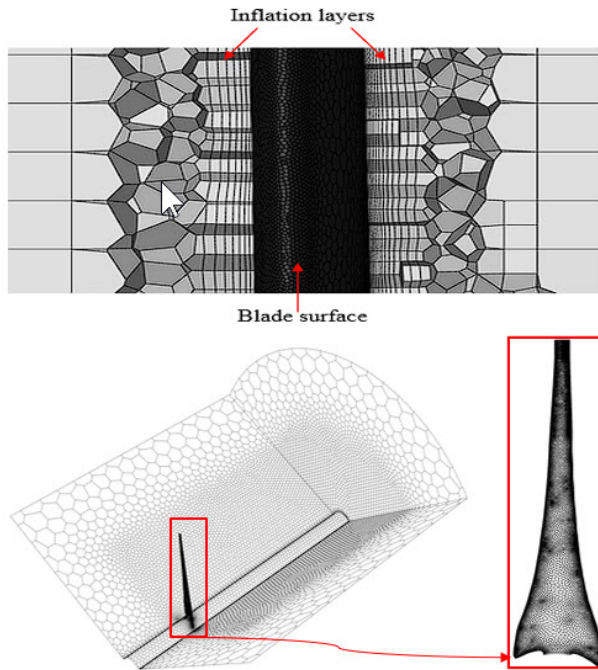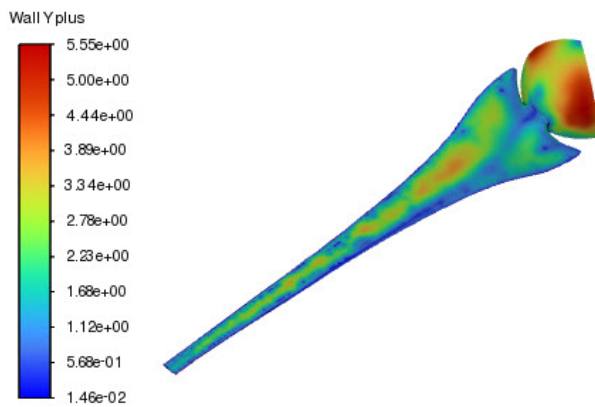
FIGURE 5. Computational mesh.

FIGURE 6. $Y+$ distribution on the blade surface.

A series of simulations were carried out to accurately model the viscous sublayer of the boundary layer to meet the requirements of the SST turbulence model, which include automatic wall treatment. To ensure that the non-dimensional parameter $y+$ stays below 1, the height of the first layer normal to the wall surface was adjusted. This was achieved by using a fine mesh in the near-wall region with a minimum of 12 prism layers perpendicular to the walls. The distribution of $y+$ on the blade surface is shown in Figure 6. The mesh resolution was suffi-cient enough to ensure that $y+$ remained within the recommended limit.

2.4. BOUNDARY CONDITIONS
After the meshes for each part have been generated in the Fluent Meshing software, the next step is to define the boundary conditions, analysis type, interfaces, etc. It is essential to define the flow variables at the boundary of the selected physical model in an appropriate manner. In this research, the fluid dynamics analysis
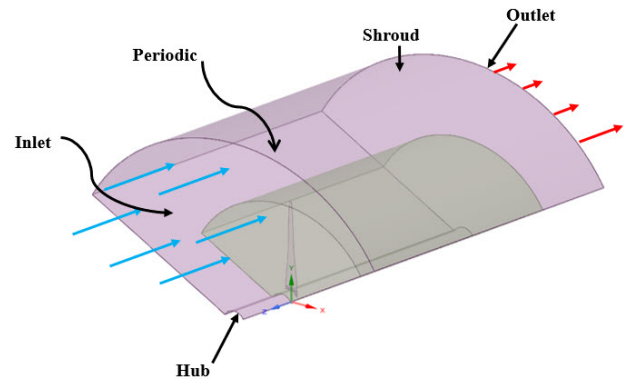

FIGURE 7. Boundary conditions in Fluent.

was carried out using the ANSYS FLUENT software during unsteady simulation, the converged solutions obtained from a steady-state simulation were used as the initial value for the unsteady simulation. The rotational speed of the rotor is $N = 400$ rpm. Based on the blade cord length, the tip speed is equal to $21.77 \, \text{m s}^{-1}$. The corresponding rotation frequency and impeller period are defined as $RF = N/60 = 6.66$ Hz and $T = 1/RF = 0.15$ s, respectively. To ensure numerical stability, a small-time step size is used, corresponding to a rotation of $2.4°$ of the impellers. In our case, a complete rotation of the impellers is performed every 150 steps, therefore, the time step size, defined as the impeller period divided by 150 steps, is equal to 0.001 s.

At the inlet of the domain, a constant velocity condition of $8 \, \text{m s}^{-1}$ was applied as a boundary condition with a turbulence intensity of $0.2 \, \%$, while the eddy viscosity was 10 and the air density was $1.2 \, \text{kg m}^{-3}$. At the arithmetic outlet, the ambient pressure was set as a boundary condition and the outlet pressure was set to zero, i.e. the external pressure, and the standard $k-\omega$ turbulence model was also chosen due to the characteristic of this model. Figure 7 shows the boundary conditions and field domains set to perform the simulation.

2.5. THE GOVERNING EQUATIONS
All fluid dynamics is based on three physical principles: the principle of conservation of mass, Newton's second law, and the principle of conservation of energy.

2.5.1. THE MASS CONSERVATION EQUATIONS
The equation for the conservation of mass, or continuity equation, can be written as follows [36]:

$$\frac{\partial \rho}{\partial t} + \nabla \cdot (\rho \vec{v}) = S_m \,. \tag{1}$$

The source S_m is the mass added to the continuous phase from the dispersed second phase and any user-defined sources.

2.5.2. MOMENTUM CONSERVATION EQUATIONS

$$\frac{\partial}{\partial t}(\rho \vec{v}) + \nabla \cdot (\rho \vec{v} \vec{v}) = -\nabla p + \nabla \cdot (\overline{\overline{\tau}}) + \rho \vec{g} + \vec{F} \,, \tag{2}$$
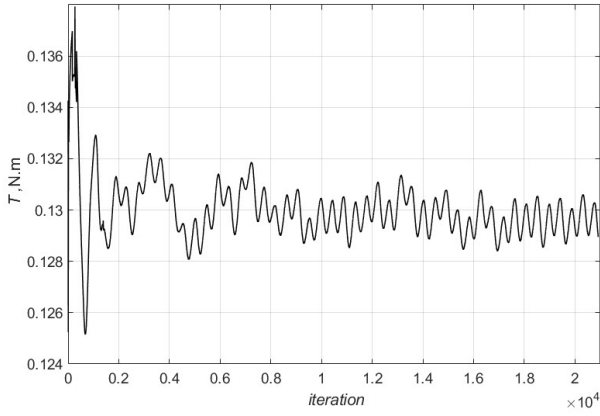
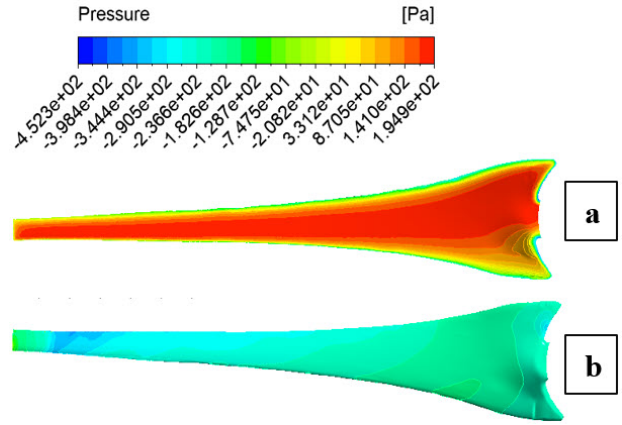FIGURE 8. Time evolution of the moment on the blade surface in the Z-axis.

FIGURE 9. Pressure contours for the 3D blade at 0.032 s; a) pressure side, b) suction side.
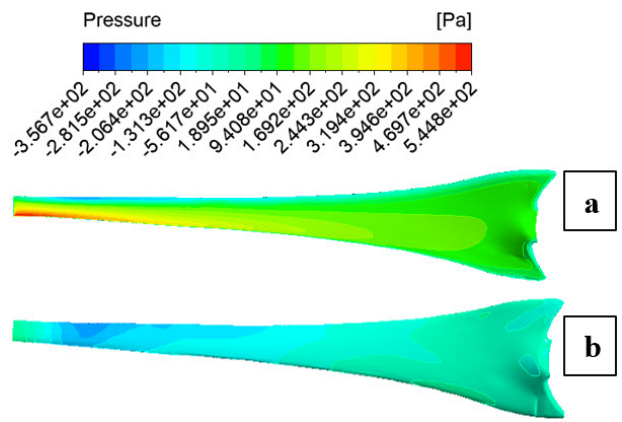
FIGURE 10. Pressure contours for the 3D blade at 0.064 s; a) pressure side, b) suction side.

where ρ is the static pressure, $\overline{\overline{\tau}}$ is the stress tensor, $\rho\overrightarrow{g}$ is the gravitational body, and $\overrightarrow{F}$ is the force and external body forces, $\overrightarrow{F}$ also includes other model-dependent source terms, such as porous-media and user-defined sources.

2.5.3. ENERGY CONSERVATION EQUATION

$$\frac{\partial}{\partial t}(\rho E) + \nabla\cdot(\overrightarrow{v}\cdot(\rho E + p)) = -\nabla\left(\sum_j h_j J_j\right) + S_h, \quad (3)$$

where h_j is the heat transfer coefficient of species j, J_j is the broadcast stream of species j, and S_h is the volumetric rate of heat generation.

2.6. REYNOLDS (ENSEMBLE) AVERAGING

In Reynolds averaging, the solution variables in the instantaneous Navier-Stokes equations are decomposed into the mean and fluctuating components [37].

$$\frac{\partial\rho}{\partial t} + \frac{\partial}{\partial x_i}(\rho u_i) = 0, \quad (4)$$

$$\frac{\partial}{\partial t}(\rho u_i) + \frac{\partial}{\partial x_i}(\rho u_i u_j) = -\frac{\partial p}{\partial x_i} +$$

$$\frac{\partial}{\partial x_j}\left[\mu\left(\frac{\partial u_i}{\partial x_j} + \frac{\partial u_l}{\partial x_l} - \frac{2}{3}\delta_{ij}\right) + \frac{\partial}{\partial x_j}(\rho\overline{u_i' u_j'})\right]. \quad (5)$$

The Reynolds-averaged Navier-Stokes (RANS) equations are Equations (4) and (5). The velocities and other solution variables now represent ensemble averaged values, but the equations retain the same overall structure as the instantaneous Navier-Stokes equations. There are now more words to describe the effects of turbulence. To complete Equation (5), these Reynolds stresses, $\rho\overline{u_i' u_j'}$, must be modeled.

3. RESULTS AND DISCUSSION

In this section, we present the results of the wind turbine blade simulation. The design of the blade follows a 120° axial symmetry approximation, taking into account the symmetric nature of the computational domain. CFD was used to perform the simulation and solve the flow governing equations (3D Navier-Stokes) around the turbine blade. In order to assess the convergence of the time-periodic results, we monitored the moment around the Z-axis during the unsteady simulation. A visual representation of the moment around the Z-axis of the blade is shown in Figure 8.

According to the graph, the unsteady solution initially shows instability but eventually transitions to periodic behaviour, indicating that the solution has converged during the unsteady simulation. To achieve this, 40 iterations were performed at each time-step, effectively reducing the residuals for continuity, momentum, and turbulence quantities below 10^{-5}. Figures 9, 10, and 11 present the distribution of air pressure on both sides of the wind turbine blade at three specific time points: 0.032, 0.064, and 0.096 s.

The pressure distribution shows significant variations at different locations along the blade of the wind turbine, with notable differences observed from the leading edge to the trailing edge and from the root to the tip on both the suction and pressure sides.

To compare the velocity field around the blade surface obtained from the numerical calculations, Fig-
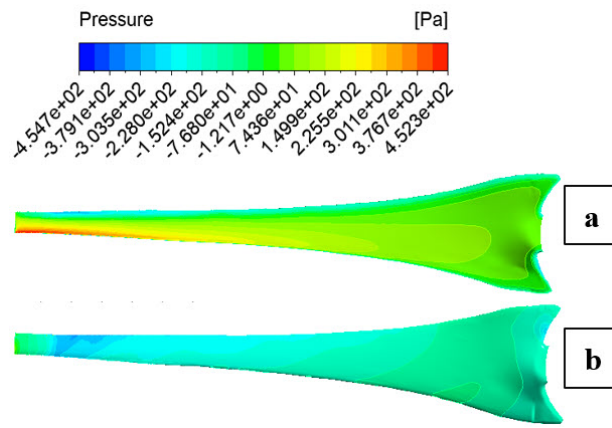
FIGURE 11. Pressure contours for the 3D blade at 0.096 s; a) pressure side, b) suction side.
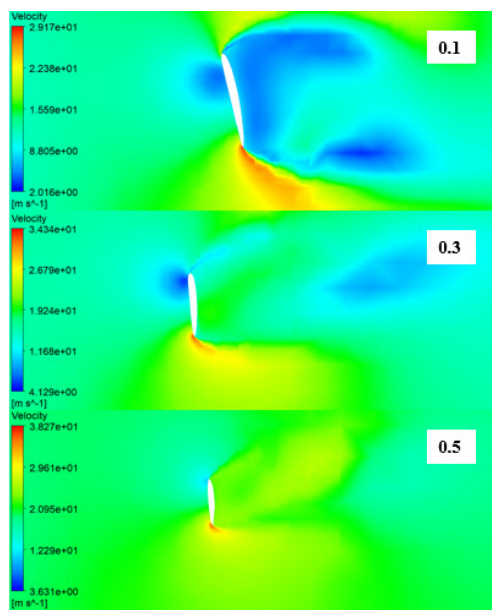

FIGURE 12. Velocity along clean wind turbine blade profile sections, 0.032 s.
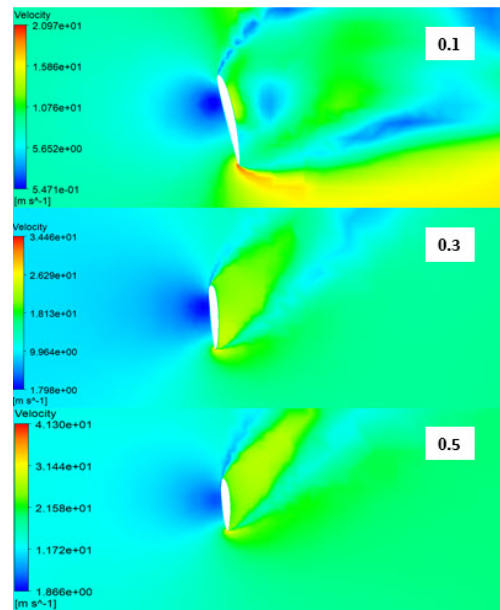

FIGURE 13. Velocity along clean wind turbine blade profile sections, 0.064 s.
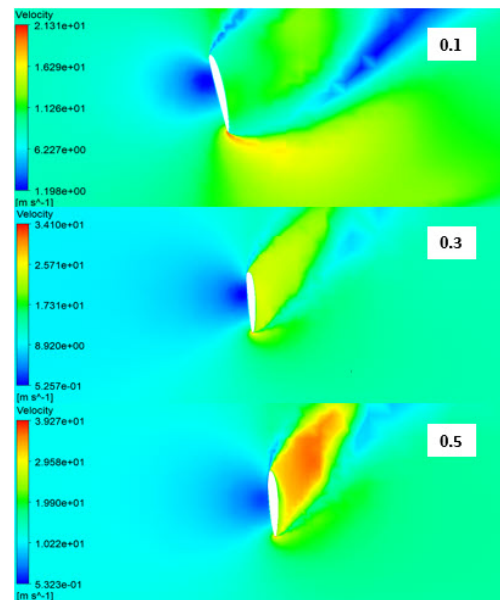
FIGURE 14. Velocity along clean wind turbine blade profile sections, 0.096 s.

ures 12, 13, and 14 show the results at a constant speed of $8 \, \mathrm{m \, s^{-1}}$. These comparisons have been made using the plane section option in the CFD post-processing, specifically in three selected sections (0.1, 0.3, and 0.5) of the 3D wind turbine blades. The figures show the results at three different time points: 0.032, 0.064, and 0.096 s.

The velocity profiles shown in the figures illustrate the velocity filed around the blade surface at three differ-ent sections (0.1, 0.3, and 0.5) of the airfoil profiles. At the time instant 0.032 s and section 0.1, the velocity at the trailing edge is higher than that at the leading edge of the airfoil, while the direction of the velocity change remains the same as in the other sections. In the remaining sections, the speed increases on the upper side. The subsequent times, 0.064 and 0.096 s, show similar velocity changes to the initial time, but with some variations in the three sections.

Furthermore, Figures 15, 16, and 17 show the pressure distribution on the airfoil coil of the wind turbine blade within three different sections (0.1, 0.3, and 0.5) at three different times: 0.032, 0.064, and 0.096 s. These figures were generated at a constant speed of $8 \, \mathrm{m \, s^{-1}}$.

From the figures, it can be clearly seen that the pressure distribution on the airfoil coil of the wind turbine blade has distinct characteristics in the selected sections: 0.1, 0.3, and 0.5 of the blade at time 0.032 s. Notably, the pressure on the upper surface is lower as compared to the lower surface, and the pressure values between the sections are relatively close.

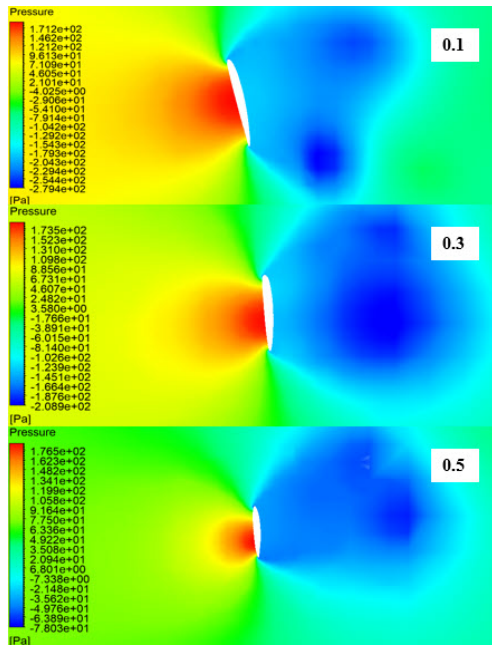However, at times 0.064 and 0.096 s, as shown in

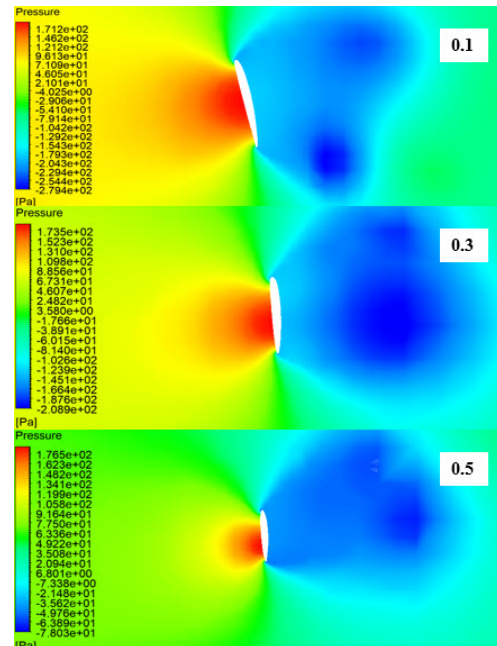Figure 15. Pressure contours along wind turbine blade profiles in 0.032 s.

Figure 16. Pressure contours along wind turbine blade profiles in 0.064 s.

Figures 16 and 17, there is a noticeable increase in the pressure distribution around the aileron. Specifically, there is an observable increase in pressure on the upper surface, particularly in the 0.5 section at both time points (0.064 and 0.096 s).

3.1. Pressure coefficients comparisons

The dimensionless pressure coefficient (C_p) was calculated by CFD numerical simulations for three specific sections (0.1, 0.3, and 0.5) of the wind turbine blades. The obtained C_p values were then compared with results from different time points, as illustrated in Figure 18. It is important to note that the pressure coefficient, being a local quantity, is a challenging test for CFD simulations. The calculation of the pressure coefficient can be computed using the provided Equation (6) [23, 25, 26].

$$C_p = \frac{2(P - P_{ref})}{\rho \cdot V_\infty^2}, \qquad (6)$$

where P is the absolute pressure across the blade profile, P_{ref} is the static pressure, ρ is the free upstream flow density and V_∞ is the free upstream flow velocity.

The pressure coefficient values show a significant level of agreement, particularly at the leading edge, across the three sections (0.1, 0.3, and 0.5) of the blade at different time points, as can be seen from the Figure 18. However, slight differences can be observed in some of the trailing edge values. These variations arise due to the influence of lift and drag forces, which impact the flow characteristics and subsequently affect the pressure coefficient (C_p) parameters.
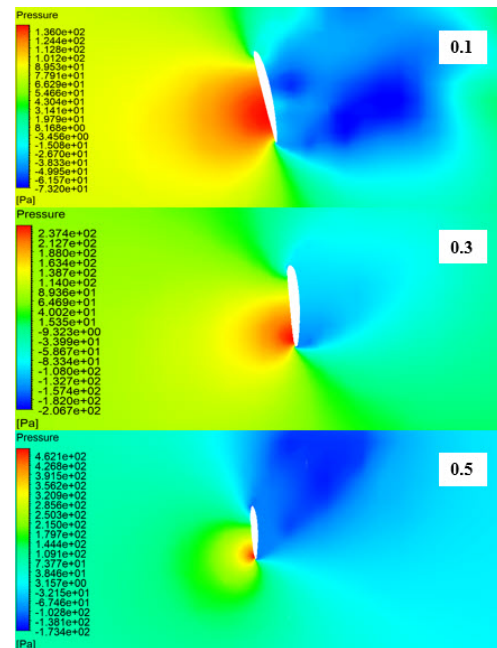

Figure 17. Pressure contours along wind turbine blade profiles in 0.096 s.

4. Conclusions

The main objective of this research paper was to investigate the unsteady three-dimensional flow behaviour on the WG/EV100 wind turbine model at three different time points. Firstly, the CAD model of the blade was reverse engineered, and then three-dimensional numerical simulations of the complete wind turbine were performed using the commercial CFD code ANSYS FLUENT. Due to the computational requirements and limitations of the available computing resources, only a single blade was considered to generate the
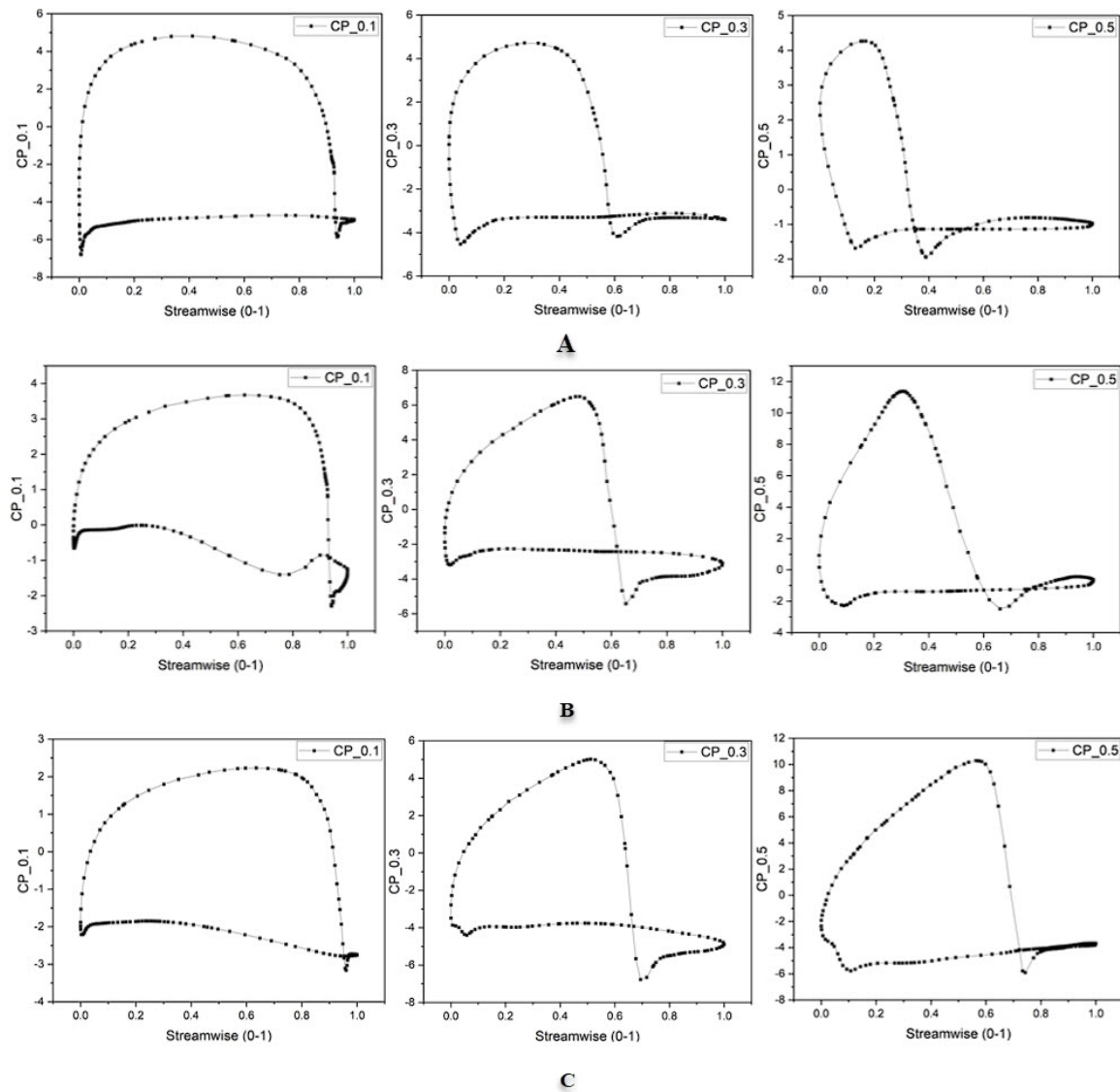
FIGURE 18. Comparison of pressure coefficients between three different times, in three sections along the blade of a wind turbine.

computational domain by taking advantage of the symmetry of the flow field. The blade was split into three sections for the same purpose of data analysis.

The pressure distribution on the blade and the velocity field on the ailerons were observed at different time points. The results show that the velocity field and the pressure distribution change over time as a result of the blade's shifting position, but the pressure coefficient remains unchanged for the three time points. When comparing the results between the three sections, namely 0.1, 0.3, and 0.5, it is found that the velocity and the pressure are greater in section 0.5, while the direction of the distribution remains the same. The simulation results in this study, particularly the analysis of pressure coefficients, provide valuable insights into the performance and design optimisation of wind turbine blades. Due to the sensitivity of the pressure coefficient to factors, such as blade profile, thickness, and torsion angle distribution,

we observed significant variations in C_p values across different sections, highlighting the importance of considering these parameters during the design process. Using the pressure coefficient values obtained, future research aims to further improve the performance of the investigated wind turbine through an improved blade design. These efforts contribute to the advancement of the wind energy and developing more efficient and sustainable renewable energy solutions.

LIST OF SYMBOLS

S_m Mass added to the continuous
ρ Density of air
p Static pressure
$\rho \overrightarrow{g}$ Gravitational body
$\overrightarrow{F}$ Force
h_j Heat transfer coefficient of species
J_j Diffusion flux
S_h Volumetric rate

REFERENCES

[1] M. N. Uddin, F. Abera. Efficiency optimisation based speed control of IPMSM drive. *International Journal of Industrial Electronics and Drives* **1**(1):34–41, 2009. https://doi.org/10.1504/IJIED.2009.025344

[2] E. H. E. Bayoumi. Stator resistance estimator for direct torque control of permanent magnet synchronous motor drive systems using multi-resolution analysis wavelet. *International Journal of Industrial Electronics and Drives* **1**(3):191–201, 2014. https://doi.org/10.1504/IJIED.2014.064092

[3] A. Tummala, R. K. Velamati, D. K. Sinha, et al. A review on small scale wind turbines. *Renewable and Sustainable Energy Reviews* **56**:1351–1371, 2016. https://doi.org/10.1016/j.rser.2015.12.027

[4] D. Rekioua. *Wind power electric systems.* Springer, London, UK, 1st edn., 2014. https://doi.org/10.1007/978-1-4471-6425-8

[5] C. Hetyei, F. Szlivka. Counter-rotating dual rotor wind turbine layout optimisation. *Acta Polytechnica* **61**(2):342–349, 2021. https://doi.org/10.14311/AP.2021.61.0342

[6] M. Shuwa, G. M. Ngala, A. M. El-jummah. Performance analysis of horizontal axis wind turbine using variable blade pitch control mechanism. *Arid Zone Journal of Engineering, Technology and Environment* **16**(1):179–187, 2020.

[7] M. Shuwa, M. G. Ngala, M. Maina. Development and performance test of a micro horizontal axis wind turbine blade. *International Journal of Engineering Research and Applications* **6**(2):11–17, 2016.

[8] G. M. Ngala, M. Shuwa. Development of a micro horizontal axis wind turbine blade for the semi-arid region of Nigeria. In *Sustainable Energy Development and Innovation: Selected Papers from the World Renewable Energy Congress (WREC)*, pp. 681–691. 2022. https://doi.org/10.1007/978-3-030-76221-6_75

[9] A. Aihara, V. Mendoza, A. Goude, H. Bernhoff. A numerical study of strut and tower influence on the performance of vertical axis wind turbines using computational fluid dynamics simulation. *Wind Energy: An International Journal for Progress and Applications in Wind Power Conversion Technology* **25**(5):897–913, 2022. https://doi.org/10.1002/we.2704

[10] J. Chen, Q. Wang, S. Zhang, et al. A new direct design method of wind turbine airfoils and wind tunnel experiment. *Applied Mathematical Modelling* **40**(3):2002–2014, 2016. https://doi.org/10.1016/j.apm.2015.09.051

[11] G. P. Demelio, S. M. Camporeale, A. Castellano, et al. Design and construction of an offshore diffuser augmented wind turbine with a high efficiency alternator. *IOP Conference Series: Materials Science and Engineering* **1214**(1):012030, 2022. https://doi.org/10.1088/1757-899X/1214/1/012030

[12] P. Fuglsang, Christian Bak. Development of the Risø wind turbine airfoils. *Wind Energy: An International Journal for Progress and Applications in Wind Power Conversion Technology* **7**(2):145–162, 2004. https://doi.org/10.1002/we.117

[13] H. Sobieczky. Parametric airfoils and wings. In *Recent development of aerodynamic design methodologies: Notes on Numerical Flid Mechanics (NNFM)*, vol. 65, pp. 71–87. 1999. https://doi.org/10.1007/978-3-322-89952-1_4

[14] Y. M. El-Okda. Design methods of horizontal axis wind turbine rotor blades. *International Journal of Industrial Electronics and Drives* **2**(3):135–150, 2015. https://doi.org/10.1504/IJIED.2015.072789

[15] M. Aladag, M. Bernacka, M. Joka-Yildiz, et al. Reverse engineering of parts with asymmetrical properties using replacement materials. *Acta Mechanica et Automatica* **16**(3):250–258, 2022. https://doi.org/10.2478/ama-2022-0030

[16] A. Filippone. Airfoil inverse design and optimization by means of viscous-inviscid techniques. *Journal of Wind Engineering and Industrial Aerodynamics* **56**(2–3):123–136, 1995. https://doi.org/10.1016/0167-6105(94)00095-U

[17] G. D. Barai, S. S. Shete, L. P. Raut. Design and development of a component by reverse engineering. *IJRET: International Journal of Research in Engineering and Technology* **4**(5):539–546, 2015. https://doi.org/10.15623/ijret.2015.0405100

[18] M. Manić, Z. Stamenković, M. Mitković, et al. Design of 3D model of customized anatomically adjusted implants. *Facta Universitatis, Series: Mechanical Engineering* **13**(3):269–282, 2015.

[19] P. Wang, J. Yang, Y. Hu, et al. Innovative design of a helmet based on reverse engineering and 3D printing. *Alexandria Engineering Journal* **60**(3):3445–3453, 2021. https://doi.org/10.1016/j.aej.2021.02.006

[20] J. F. Manwell, J. G. McGowan, A. L. Rogers. *Wind energy explained: Theory, design and application.* John Wiley & Sons, Chichester, UK, 2nd edn., 2010.

[21] H. Al-Qarishey, R. W. Fletcher, E. A. Alkareem. Computational fluid dynamics turbulence and wake study of a utility-scale rotating three-blade horizontal axis wind turbine. In *Proceedings of the ASME International Mechanical Engineering Congress and Exposition*, vol. 8B, p. V08BT08A026. 2021. https://doi.org/10.1115/IMECE2021-70095

[22] I. A. Abdelrahman, M. Y. Mahmoud, M. M. Abdelfattah, et al. Computational and experimental investigation of lotus-inspired horizontal-axis wind turbine blade. *Journal of Advanced Research in Fluid Mechanics and Thermal Sciences* **87**(1):52–67, 2021. https://doi.org/10.37934/arfmts.87.1.5267

[23] S. Merryisha, P. Rajendran. Experimental and CFD analysis of surface modifiers on aircraft wing: A review. *CFD Letters* **11**(10):46–56, 2019.

[24] C. J. Bai, F. B. Hsiao, M. H. Li, et al. Design of 10 kW horizontal-axis wind turbine (HAWT) blade and aerodynamic investigation using numerical simulation. *Procedia Engineering* **67**:279–287, 2013. https://doi.org/10.1016/j.proeng.2013.12.027

[25] N. A. Mezaal, K. V. Osintsev, S. V. Alyukov. The computational fluid dynamics performance analysis of horizontal axis wind turbine. *International Journal of Power Electronics and Drive Systems* **10**(2):1072–1080, 2019. `https://doi.org/10.11591/ijpeds.v10.i2.pp1072-1080`

[26] P. I. Muiruri, O. S. Motsamai. Three dimensional CFD simulations of a wind turbine blade section; Validation. *Journal of Engineering Science & Technology Review* **11**(1):138–145, 2018. `https://doi.org/10.25103/jestr.111.16`

[27] I. Paraschivoiu, F. Delclaux. Double multiple streamtube model with recent improvements (for predicting aerodynamic loads and performance of Darrieus vertical axis wind turbines). *Journal of Energy* **7**(3):250–255, 1983. `https://doi.org/10.2514/3.48077`

[28] Y. El-khchine, M. Sriti. Performance prediction of a horizontal axis wind turbine using BEM and CFD methods. *MATEC Web of Conferences* **45**:05005, 2016. `https://doi.org/10.1051/matecconf/20164505005`

[29] M. Hasan, A. El-Shahat, M. Rahman. Performance investigation of three combined airfoils bladed small scale horizontal axis wind turbine by BEM and CFD analysis. *Journal of Power and Energy Engineering* **5**(5):14–27, 2017. `https://doi.org/10.4236/jpee.2017.55002`

[30] M. Khaled, M. M. Ibrahim, H. E. A. Hamed, A. F. A. Gawad. Aerodynamic design and blade angle analysis of a small horizontal-axis wind turbine. *American Journal of Modern Energy* **3**(2):23–37, 2017. `https://doi.org/10.11648/j.ajme.20170302.12`

[31] M. Chandrala, A. Choubey, B. Gupta. Aerodynamic analysis of horizontal axis wind turbine blade. *International Journal of Engineering Research and Applications (IJERA)* **2**(6):1244–1248, 2012.

[32] N. Khlaifat, A. Altaee, J. Zhou, et al. Optimization of a small wind turbine for a rural area: A case study of Deniliquin, New South Wales, Australia. *Energies* **13**(9):2292, 2020. `https://doi.org/10.3390/en13092292`

[33] A. Rossetti, G. Pavesi. Comparison of different numerical approaches to the study of the H-Darrieus turbines start-up. *Renewable Energy* **50**:7–19, 2013. `https://doi.org/10.1016/j.renene.2012.06.025`

[34] J. Zhang, J. Wang, S. Yan. The effect of yaw speed and delay time on power generation and stress of a wind turbine. *International Journal of Green Energy* **20**(2):153–165, 2023. `https://doi.org/10.1080/15435075.2021.2023884`

[35] R. Udroiu. Research regarding reverse engineering for aircraft components. *MATEC Web of Conferences* **94**:01012, 2017. `https://doi.org/10.1051/matecconf/20179401012`

[36] H. Park, J. Roh, K. C. Oh, et al. Modeling and optimization of water mist system for effective air-cooled heat exchangers. *International Journal of Heat and Mass Transfer* **184**:122297, 2022. `https://doi.org/10.1016/j.ijheatmasstransfer.2021.122297`

[37] ANSYS, Inc. Ansys fluent theory guide. *Ansys Inc, USA* **15317**:724–746, 2011.